Nanoscale magnetic resonance imaging

C. L. Degen[a], M. Poggio[a,b], H. J. Mamin[a], C. T. Rettner[a], and D. Rugar[a,1]

[a]IBM Research Division, Almaden Research Center, 650 Harry Road, San Jose, CA 95120; and [b]Center for Probing the Nanoscale, Stanford University, 476 Lomita Mall, Stanford, CA 94305

Communicated by Stuart S. P. Parkin, IBM Almaden Research Center, San Jose, CA, December 1, 2008 (received for review August 21, 2008)

We have combined ultrasensitive magnetic resonance force microscopy (MRFM) with 3D image reconstruction to achieve magnetic resonance imaging (MRI) with resolution <10 nm. The image reconstruction converts measured magnetic force data into a 3D map of nuclear spin density, taking advantage of the unique characteristics of the "resonant slice" that is projected outward from a nanoscale magnetic tip. The basic principles are demonstrated by imaging the ^{1}H spin density within individual tobacco mosaic virus particles sitting on a nanometer-thick layer of adsorbed hydrocarbons. This result, which represents a 100 million-fold improvement in volume resolution over conventional MRI, demonstrates the potential of MRFM as a tool for 3D, elementally selective imaging on the nanometer scale.

MRFM | MRI | nuclear magnetic resonance | molecular structure imaging

Magnetic resonance imaging (MRI) is well-known in medicine and in the neurosciences as a powerful tool for acquiring 3D morphological and functional information with resolution in the millimeter-to-submillimeter range (1, 2). Unfortunately, despite considerable effort, attempts to push the spatial resolution of conventional MRI into the realm of high-resolution microscopy have been stymied by fundamental limitations, especially detection sensitivity (3, 4). Consequently, the highest resolution MRI microscopes today remain limited to voxel volumes >40 μm^3 (5–8). The central issue is that MRI is based on the manipulation and detection of nuclear magnetism, and nuclear magnetism is a relatively weak physical effect. It appears that conventional coil-based inductive detection techniques simply cannot provide adequate signal-to-noise ratio for detecting voxel volumes below the micrometer size. This sensitivity constraint is unfortunate because MRI has much to offer the world of microscopy with its unique contrast modalities, its elemental selectivity, and its avoidance of radiation damage.

Despite the many challenges, there is strong motivation to extend MRI to finer resolution, especially if the nanometer scale can be reached. At the nanometer scale, one might hope to directly and nondestructively image the 3D structure of individual macromolecules and molecular complexes (9). Such a powerful molecular imaging capability could be of particular interest to structural biologists trying to unravel the structure and interactions of proteins, especially for those proteins that cannot be crystallized for X-ray analysis, or are too large for conventional NMR spectroscopy. Nanoscale MRI, with its capacity for true 3D, subsurface imaging, its potential for generating contrast by selective isotopic labeling and its nondestructive nature, would be a welcome complement to the characteristics of electron microscopy. The key to pushing MRI to the nanoscale is detection sensitivity.

Recently, a significant breakthrough in magnetic resonance detection sensitivity has been achieved by using magnetic resonance force microscopy (MRFM) (9–13), resulting in single spin detection for electrons (14) and substantial progress in nuclear spin detection (15–24). Despite the great progress in nuclear spin MRFM, only one previous nanoscale imaging experiment has been demonstrated, and it was limited to 90-nm resolution in 2 dimensions for ^{19}F nuclei in an inorganic test sample (25). Here, we report that MRFM can perform 3D MRI of ^{1}H nuclear spins (protons) in a biological specimen [tobacco mosaic virus (TMV) particles] with a spatial resolution down to 4 nm. This capability is enabled by several key technical advances, including the generation of magnetic field gradients as high as 4 million Tesla (T) per meter, detailed understanding of the MRFM point-spread function, and application of an image-reconstruction technique capable of converting magnetic force measurements into a 3D map of proton density.

Principles

MRFM is based on mechanical measurement of ultrasmall (attonewton) magnetic forces between nuclear spins in a sample and a nearby magnetic tip. Basic elements of our MRFM apparatus are shown in Fig. 1. The test sample consists of individual TMV particles that are deposited onto the flat end of an ultrasensitive silicon cantilever. The end of the cantilever is positioned close to a 200-nm-diameter magnetic tip that produces a strong and very inhomogeneous magnetic field. The magnetic tip sits on a copper "microwire" that serves to efficiently generate a radiofrequency (rf) magnetic field that excites NMR (26). Frequency modulation of the rf field induces periodic inversions of the ^{1}H spins in the sample, resulting in a periodic force that drives the mechanical resonance of the cantilever. Monitoring the cantilever oscillation amplitude while mechanically scanning the magnetic tip with respect to the sample in 3 dimensions provides data that allow the reconstruction of the ^{1}H density. The imaging is performed in vacuum and at low temperature (T = 300 mK).

The TMV particles are deposited onto the cantilever in solution and then air dried. (See supporting information (SI) *Appendix* for preparation details.) As shown in Fig. 1*B*, the sample consists of both whole virus and smaller fragments. The TMV particles, which have a rod-like geometry with diameter of 18 nm and lengths up to 300 nm (27, 28), were chosen as test objects because they are physically robust and have a size suitable for evaluating our imaging resolution. They also serve to demonstrate that MRFM is capable of imaging native biological specimens. Approximately 95% of the virus mass consists of protein, resulting in a ^{1}H density estimated to be $\rho = 4 \times 10^{28}$ spins per m^3. In the future, rapid freezing techniques, such as used in cryoelectron microscopy, could be used to better preserve the structural integrity of fully hydrated biological samples (29, 30).

NMR will only occur if the ^{1}H spins in the sample are at the correct field for satisfying the Larmor resonance condition: $B_0(\mathbf{r}) = \omega_0/\gamma \equiv B_{\text{res}}$, where ω_0 is the rf field frequency, and $\gamma = 2\pi \times 42.57$ MHz/T is the proton gyromagnetic ratio. The field $B_0(\mathbf{r}) \equiv |B_{\text{ext}}\hat{\mathbf{z}} + \mathbf{B}_{\text{tip}}(\mathbf{r})|$ is supplied by the combination of the field from an external superconducting magnet, B_{ext}, and the field from the magnetic tip, $\mathbf{B}_{\text{tip}}(\mathbf{r})$, where $\mathbf{r}$ is the position with

Author contributions: C.L.D., M.P., H.J.M., and D.R. designed research; C.L.D., M.P., H.J.M., and D.R. performed research; C.T.R. contributed new reagents/analytic tools; C.L.D., M.P., H.J.M., and D.R. analyzed data; and C.L.D., M.P., and D.R. wrote the paper.

The authors declare no conflict of interest.

Freely available online through the PNAS open access option.

[1]To whom correspondence should be addressed. E-mail: rugar@almaden.ibm.com.

This article contains supporting information online at www.pnas.org/cgi/content/full/0812068106/DCSupplemental.

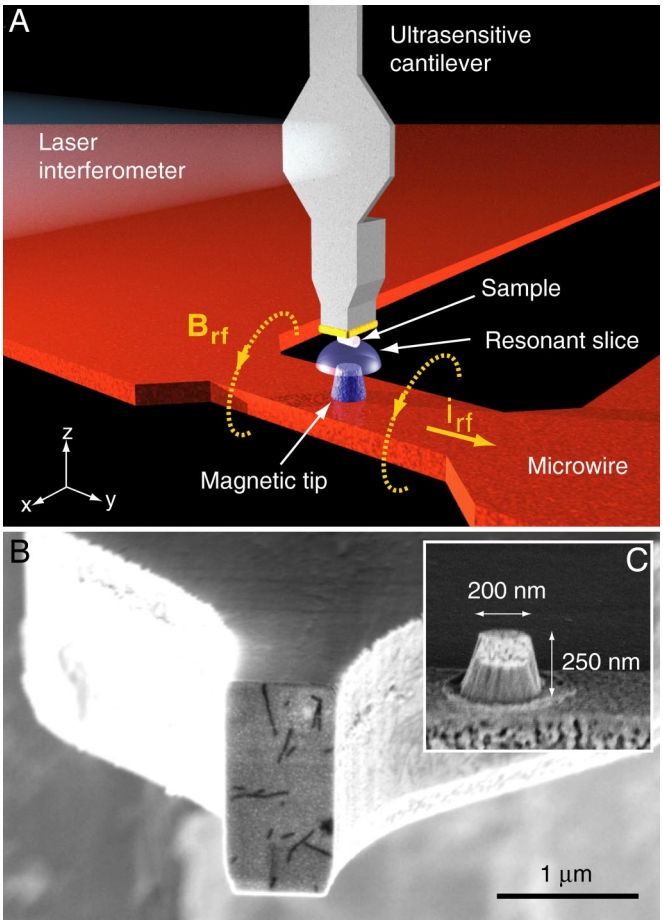

Fig. 1. Configuration of MRFM apparatus. (*A*) Tobacco mosaic virus particles, attached to the end of an ultrasensitive silicon cantilever, are positioned close to a magnetic tip. A rf current i_{rf} passing through a copper microwire generates an alternating magnetic field B_{rf} that induces magnetic resonance in the ^{1}H spins of the virus particles. The resonant slice represents those points in space where the field from the magnetic tip (plus an external field) matches the condition for magnetic resonance. Three-dimensional scanning of the tip with respect to the cantilever, followed by image reconstruction is used to generate a 3D image of the spin density in the virus sample. (*B*) Scanning electron micrograph of the end of the cantilever. Individual tobacco mosaic virus particles are visible as long, dark rods on the 0.8-μm $\times$ 1.3-μm-sized sample platform. (*C*) Detail of the magnetic tip.

respect to the tip apex. For an rf center frequency of $\omega_0 = 2\pi \times$ 114.8 MHz, the resonance condition is met for $B_0(\mathbf{r}) = 2.697$ T. Because the field from the magnetic tip is a strong function of position, the resonance is confined to a thin, approximately hemispherical "resonant slice" that extends outward from the tip (Figs. 1*A* and 2). The field gradient at the resonant slice can exceed 4×10^6 T/m at a distance of 25 nm from the tip, resulting in a slice thickness that is as thin as a few nanometers. The rf field is frequency modulated with a peak deviation of $\Delta\omega_{rf,peak} = 2\pi \times$ 600 kHz in order to drive adiabatic inversions of the protons. The periodicity of the spin inversion is chosen to match the mechanical resonance of the cantilever ($\approx$2.9 kHz). In the presence of the field gradient from the magnetic tip, the spin inversions generate a small oscillating force, typically on the order of 10 aN-rms, that excites a slight (subangstrom) vibration of the cantilever. The vibration is detected by a fiber-optic interferometer and lock-in amplifier.

The spin signal originates from the naturally occurring $\sqrt{N}$ statistical polarization of the spin ensemble ("spin noise"), where N is the number of ^{1}H spins in the measurement volume (19, 23, 31–33). Using the statistical polarization is advantageous because its root-mean-square amplitude exceeds the mean Boltzmann polarization for nanoscale volumes of spins (23). Statistical polarization is also convenient because there is no need to wait a spin-lattice relaxation time T_1 for the spins to polarize. Because the statistical polarization can be either positive or negative, we detect the signal power (i.e., the spin signal variance), which is proportional to the density of ^{1}H in the sample. We use the term "spin signal" to mean the estimated variance of the force that has spin origin, with units of aN^2. See ref. 23 and *SI Appendix* for additional details of the signal acquisition.

Three-dimensional imaging of the sample requires 2 steps: data collection and image reconstruction. First, the spin signal is measured as the magnetic tip is mechanically scanned with respect to the sample in a 3D raster pattern, yielding a map of the spin signal as a function of tip position. Because of the extended geometry of the resonant slice, however, a spatial scan does not directly produce a map of the proton distribution in the sample. Instead, each data point in the scan contains spin signal contributions from a variety of depths and lateral positions. Specifically, the map $\xi(\mathbf{r}_s)$ of the signal as a function of tip scan position $\mathbf{r}_s$ is related to the proton distribution $\rho(\mathbf{r})$ by the convolution integral

$$\xi(\mathbf{r}_s) = \int_{\substack{\text{sample}\\\text{volume}}} d^3\mathbf{r}\, K(\mathbf{r}_s - \mathbf{r})\rho(\mathbf{r}), \qquad [1]$$

where $K(\mathbf{r})$ is the 3D point spread function (PSF) associated with the resonant slice. $K(\mathbf{r})$ is defined as the mean spin signal generated by a randomly polarized spin in the sample at a position $\mathbf{r}$ with respect to the magnetic tip.

The amplitude of the MRFM point-spread function is set by 2 main factors: one that determines the effectiveness of the spin inversions and confines the response to the near vicinity of the resonant slice and one that reflects the strength of the lateral field gradient at the position of the spin. As discussed in the *SI Appendix*, we find that the PSF can be approximated by

$$K(\mathbf{r}) = \begin{cases} A\mu^2[G(\mathbf{r})]^2\left[1 - \left(\dfrac{\Delta B_0(\mathbf{r})}{\Delta\omega_{rf,peak}/\gamma}\right)^2\right] & \text{for} |\Delta B_0(\mathbf{r})| \le \Delta\omega_{rf,peak}/\gamma \\ 0 & \text{for} |\Delta B_0(\mathbf{r})| > \Delta\omega_{rf,peak}/\gamma \end{cases} \qquad [2]$$

Here, $G(\mathbf{r}) \equiv \partial B_{tip,z}/\partial x$ is the lateral field gradient from the tip, $\Delta B_0(\mathbf{r}) \equiv B_0(\mathbf{r}) - \omega_0/\gamma$ is the off-resonance condition, and $\Delta\omega_{rf,peak}/\gamma \approx 14$ mT is the peak FM modulation converted to magnetic field units. The proportionality constant A depends on details of the experiment, such as the correlation time of the spin inversions and the bandwidth of the detection. $G(\mathbf{r})$ and $B_0(\mathbf{r})$ are key components of $K(\mathbf{r})$, and both require detailed knowledge of the field produced by the magnetic tip. As discussed in *SI Appendix*, we calculate $\mathbf{B}_{tip}(\mathbf{r})$ using a magnetostatic model of the tip and then tune the parameters of the model (for example, tip magnetization and geometry) to be consistent with the measured scan data. Based on Eq. **2** and our best estimates of the magnetic tip parameters, we obtain the PSF shown in Fig. 2. At a distance of 24 nm, where the peak gradient is $G = 4.2$ mT/nm, we find the shell thickness (full width at half maximum) to be as thin as $\sqrt{2}\Delta\omega_{rf,peak}/\gamma G = 4.8$ nm.

To recover the real-space proton distribution $\rho(\mathbf{r})$ from the 3D scan data $\xi(\mathbf{r}_s)$, the effect of the PSF must be deconvolved. We use an iterative Landweber algorithm that starts with an initial

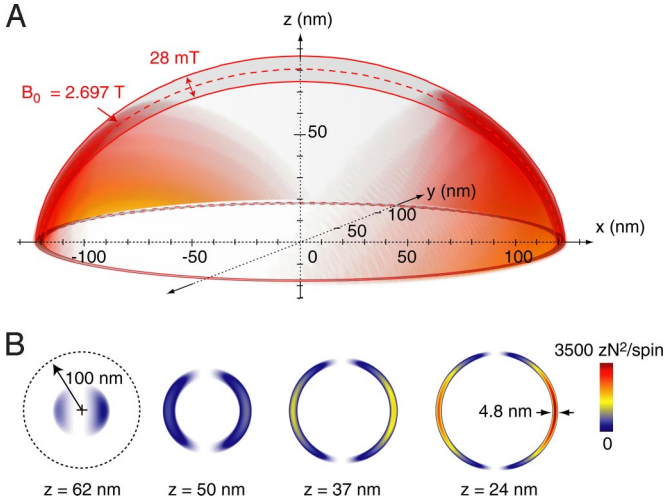

Fig. 2. Details of the resonant slice and associated point spread function (PSF). (*A*) Three-dimensional representation corresponding to the conditions $B_{res} = \omega_0/\gamma = 2.697$ T and $B_{ext} = 2.482$ T. The center of the tip apex is assumed to be at the origin of the coordinate system. The resonant slice is the hemispherical "shell" outlined in red, representing the region of space for which $B_0(\mathbf{r})$ lies within $B_{res} \pm \Delta\omega_{rf,peak}/\gamma$ (here 2.697 ± 0.014 T). Regions to the left and right of the tip (shaded red) contribute most to the signal because this is where the lateral gradient $G(\mathbf{r})$ is largest. (*B*) Cross-sections of the point spread function at the 4 tip-sample spacings used in the imaging experiment. The PSF was calculated by using Eq. **2**, assuming $A = 1$. The color scale reflects the force variance per spin (zN = zeptonewton = 10^{-21} N). The size of the tip apex (r_a = 100 nm) is indicated by a dotted circle. At $z = 24$ nm, the PSF lobe thickness reaches a minimum of ≈4.8 nm (FWHM). The small left–right asymmetry is due to a slight (1.7°) tilt of the sample plane with respect to the magnetic tip.

estimate for the spin density of the object, $\rho_0(\mathbf{r})$ and then improves the estimate successively by using the following steps (34, 35):

$$\delta\xi_n(\mathbf{r}_s) = \xi(\mathbf{r}_s) - \int_{\text{sample volume}} d^3\mathbf{r}\, K(\mathbf{r}_s - \mathbf{r})\rho_n(\mathbf{r}), \qquad [3]$$

$$\rho_{n+1}(\mathbf{r}) = \rho_n(\mathbf{r}) + \alpha(\mathbf{r}) \int_{\text{scan volume}} d^3\mathbf{r}_s\, K(\mathbf{r}_s - \mathbf{r})\delta\xi_n(\mathbf{r}_s), \qquad [4]$$

where $\rho_n(\mathbf{r})$ is the reconstructed spin density after n iterations, $\delta\xi_n(\mathbf{r}_s)$ is the difference between the measured and predicted spin signal maps (the error to be minimized), and $\alpha(\mathbf{r})$ controls the rate of convergence. Because spin density should always be ≥ 0, we enforce this condition by setting any negative values of $\rho_n(\mathbf{r})$ to zero after each iteration step. The iterations typically proceed for a few thousand steps until the residual error becomes comparable with the measurement noise. In the future, the implementation of more sophisticated image reconstruction algorithms may be advantageous (36).

Results

Fig. 3A shows 3D scan data organized as *x*–*y* scans taken at 4 different tip-sample spacings: d = 24, 37, 50, and 62 nm. Each of the approximately 50-nm × 50-nm scan areas contains 60 × 32 data points acquired with an acquisition time of 1 min per point. Peak signal strength ranged from ≈600 aN^2 for the closest scan plane to ≈90 aN^2 at the most distant plane. The uncertainty of the spin signal estimate (the standard error of the measurement) ranges from ≈40 aN^2 for the d = 24 nm scan plane to ≈15 aN^2 for d = 62 nm. Thus, at the positions of maximum signal, the signal-to-noise ratio (SNR) varied from ≈15 for the closest scan plane to ≈6 at the most distant plane.

The correlation time τ_m of the spin signal was estimated from the signal bandwidth and found to be quite short, on the order of 20 ms. This is significantly shorter than has been seen in some inorganic test samples (26), possibly because of a naturally short rotating frame relaxation time $T_{1\rho}$.

An indication of the spatial resolution inherent in the raw data can be seen in the line scan shown in Fig. 3*B*. The line scan, taken with d = 24 nm tip-sample spacing, shows a background spin signal of ≈300 aN^2, with signal peaks up to ≈600 aN^2. The leading edges of the peaks are sharp and indicate that the resolution in the x direction (before deconvolution) is on the order of 4 nm, which is approximately the thickness of the resonant slice (Fig. 2*B*).

Perhaps the most striking aspects of Fig. 3*A* are the apparent "double" images in each of the *x*–*y* scans. This feature doubling effect is due to the 2-lobed character of the PSF (Fig. 2*B*). As expected, the feature pairs are seen to move apart as the tip-sample spacing decreases.

The signal information from the 4 scan planes (together with a fifth "zero" plane at d = 75 nm, where no signal was found to be present) constitutes a 3D dataset that can be deconvolved to find the real-space image of the spin density. The result of the deconvolution is displayed in Fig. 3*C*, which shows the calculated spin density of the sample as a series of *x*–*y* planes at various *z* positions. A representative *x*–*y* plane is highlighted in Fig. 3*D* and clearly shows an assembly of a few individual virus particles (mostly fragments). Given that the raw MRFM data are spatially undersampled and have only modest SNR, the quality of the reconstruction is remarkable. The observation of significant improvement in image SNR after reconstruction is expected because most spins contribute force signal to more than one position in the scan, and the cumulative effect benefits the SNR of the reconstruction. The resolution appears to be in the 4- to 10-nm range, depending on the direction, with the x direction having the highest resolution. This resolution anisotropy is expected because of the directional dependence of the PSF, which reflects the fact that the cantilever responds only to the x component of magnetic force.

The fidelity of the MRFM reconstruction is confirmed by comparing the results in Fig. 3*D* to the scanning electron microscope (SEM) image of the same sample region (Fig. 3*E*). Excellent agreement is found even down to small details. Note that the origin of contrast in the 2 images is qualitatively very different. The MRFM reconstruction is elementally specific and shows the 3D distribution of hydrogen in the sample. Contrast in the SEM image is mainly due to the virus blocking the secondary electrons emitted from the underlying gold-coated cantilever surface.

The depth resolution that is enabled by the 3D image reconstruction is illustrated in Fig. 3*F*, which shows a vertical cross-section that extends through 2 virus fragments. Interestingly, the cross-sectional cut reveals that the virus particles sit on top of a thin layer of proton-containing material that is not visible by SEM. The presence of this background layer is not surprising because it is well known that surfaces that have been exposed to ordinary laboratory air become coated with a thin layer of adsorbed hydrocarbons and water. It is this proton-rich layer that is responsible for the 300 aN^2 baseline signal in Fig. 3*B*. Taking this baseline signal level, combined with knowledge of the point-spread function and the typical spin density of hydrocarbons, one can estimate the layer thickness. Assuming a hydrocarbon spin density of $\rho = 7 \times 10^{28}$ spins per m^3, the layer thickness is on the order of a nanometer.

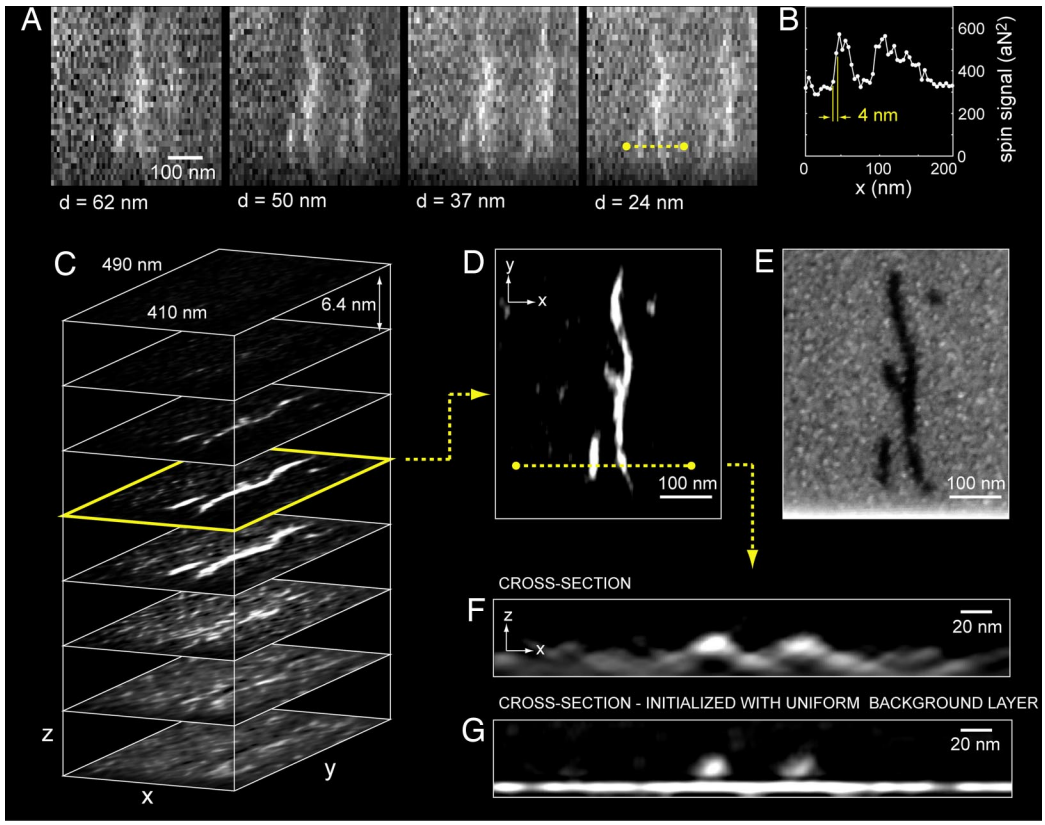

Fig. 3. Spin signal scan data and resulting 3D reconstruction of the hydrogen (proton) density distribution. (*A*) Raw scan data presented as *x*–*y* scans of the spin signal at 4 different tip-sample spacings. Pixel spacing is 8.3 nm × 16.6 nm in *x* × *y*, respectively. Each data point represents the spin signal variance obtained during a 1-min integration. B_{ext} = 2.482 T. (*B*) A more finely sampled line scan showing 4-nm lateral resolution. The scanned region is indicated by the dashed line in *A*. B_{ext} = 2.432 T. (*C*) Reconstructed 3D ^{1}H spin density. Black represents very low or zero density of hydrogen, whereas white is high hydrogen density. The image is the result of the Landweber reconstruction, followed by a 5-nm smoothing filter. (*D*) Horizontal slice of *C*, showing several TMV fragments. (*E*) Scanning electron micrograph of the same region. (*F*) Cross-section showing 2 TMV particles on top of a hydrogen-rich background layer adsorbed on the Au surface. (*G*) Reconstruction is improved if this background layer is included as a priori information by assuming a thin, uniform plane of ^{1}H density as the starting point of the reconstruction.

The reconstructions shown in Fig. 3 *C*, *D*, and *F* use no a priori knowledge of the imaged object, such as the presence of the adsorbate layer on the sample. We find that the inclusion of this information into our initial guess of the spin density ρ_0 substantially improves the result of the reconstruction. For Fig. 3*G*, we initialize ρ_0 with a uniform layer of material positioned at the level of the cantilever surface, just below the virus particle. As seen in the figure, this modification allows for a much better separation of the background layer and more clearly resolves the TMV particles. Such constraints on ρ_0 (or ρ) offer a general way to systematically include known structural information about the object.

A second MRFM image reconstruction from a neighboring sample area is shown in Fig. 4. Again, a clear 3D view of the hydrogen distribution is seen, including good spatial discrimination between the virus particles and the underlying adsorbed layer.

Discussion

We believe the present work represents substantial progress in developing the capability to probe the 3D chemical/elemental composition of nanostructures. With further progress in resolution and sample preparation, force-detected MRI techniques could have significant impact on the imaging of nanoscale biological structures, even down to the scale of individual molecules. Achieving resolution <1 nm seems realistic because the current apparatus operates almost a factor of 10 away from the best demonstrated force sensitivities (37) and field gradients (38).

Even with a resolution >1 nm, MRFM may allow the basic structure of large molecular assemblies to be elucidated. One can imagine enhancing MRFM image contrast beyond the basic spin-density information by using techniques similar to those

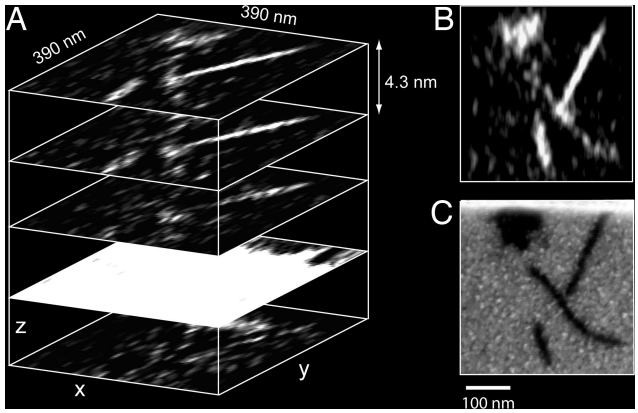

Fig. 4. Imaging results for a second sample region. (*A*) Three-dimensional reconstruction of ^{1}H spin density for virus particles sitting on adsorbed layer of hydrocarbons. (*B*) Representative horizontal slice from the 3D reconstruction showing the distribution of hydrogen in the plane located 13 nm above the hydrocarbon layer. Several virus particles are evident. (*C*) Corresponding scanning electron micrograph.

developed for clinical MRI and NMR spectroscopy. Such contrast may include selective isotopic labeling (for example, substituting ^{1}H with ^{2}H), selective imaging of different chemical species (like ^{13}C, ^{15}N, or ^{31}P), relaxation-weighted imaging, and spectroscopic imaging that reflects the local chemical environment (20, 39). Some techniques, such as cross-polarization and depolarization between different nuclear spin species, have already been demonstrated for MRFM on the micrometer scale (21, 22). At the nanometer scale, the ability to target and locate specific proteins although selective labeling, for example, could allow direct 3D imaging of the organization and structure of multicomponent macromolecular complexes. Such a capability would be complementary to current techniques, such as cryo-electron microscopy, and could develop into a powerful tool for structural biology.

ACKNOWLEDGMENTS. We thank C. Micheel, G. Wallraff, J. Cha, and S. Swanson for help with sample preparation; J. Frommer for AFM support; M. Hart and M. Farinelli for fabrication of the microwire and magnetic tip; M. Ting and A. Hero for discussions on image reconstruction; and B. Chui for cantilever fabrication. This work was supported by IBM and the National Science Foundation-funded Center for Probing the Nanoscale (National Science Foundation Grant Number PHY-0425897). C.L.D. acknowledges support from the Swiss National Science Foundation.

1. Mansfield P (2004) Snapshot magnetic resonance imaging (Nobel lecture). *Angew Chem Int Ed Engl* 43:5456–5464.
2. Buxton RB (2002) *Introduction to Functional Magnetic Resonance Imaging: Principles and Techniques* (Cambridge Univ Press, Cambridge, UK).
3. Callaghan PT (1991) *Principles of Nuclear Magnetic Resonance Microscopy* (Oxford Univ Press, Oxford), pp 173–226.
4. Glover P, Mansfield P (2002) Limits to magnetic resonance microscopy. *Rep Prog Phys* 65:1489–1511.
5. Lee SC, *et al.* (2001) One micrometer resolution NMR microscopy. *J Magn Reson* 150:207–213.
6. Ciobanu L, Seeber DA, Pennington CH (2002) 3D MR microscopy with resolution 3.7 μm by 3.3 μm by 3.3 μm. *J Magn Reson* 158:178–182.
7. Ciobanu L, Webb AG, Pennington CH (2003) Magnetic resonance imaging of biological cells. *Prog Nucl Magn Reson Spectrosc* 42:69–93.
8. Tyszka JM, Fraser SE, Jacobs RE (2005) Magnetic resonance microscopy: Recent advances and applications. *Curr Opin Biotechnol* 16:93–99.
9. Sidles JA, *et al.* (1995) Magnetic resonance force microscopy. *Rev Mod Phys* 67:249–265.
10. Sidles JA (1992) Folded Stern–Gerlach experiment as a means for detecting nuclear magnetic resonance in individual nuclei. *Phys Rev Lett* 68:1124–1127.
11. Rugar D, Yannoni CS, Sidles JA (1992) Mechanical detection of magnetic resonance. *Nature* 360:563–566.
12. Rugar D, *et al.* (1994) Force detection of nuclear magnetic resonance. *Science* 264:1560–1563.
13. Zhang Z, Hammel PC, Wigen PE (1996) Observation of ferromagnetic resonance in a microscopic sample using magnetic resonance force microscopy. *Appl Phys Lett* 68:2005–2007.
14. Rugar D, Budakian R, Mamin HJ, Chui BW (2004) Single spin detection by magnetic resonance force microscopy. *Nature* 430:329–332.
15. Züger O, Hoen ST, Yannoni CS, Rugar D (1996) Three-dimensional imaging with a nuclear magnetic resonance force microscope. *J Appl Phys* 79:1881–1884.
16. Klein O, Naletov VV, Alloul H (2000) Mechanical detection of nuclear spin relaxation in a micron-size crystal. *Eur Phys J B* 17:57–68.
17. Thurber KR, Harrell LE, Smith DD (2003) 170nm nuclear magnetic resonance imaging using magnetic resonance force microscopy. *J Magn Reson* 162:336–340.
18. Garner SR, *et al.* (2004) Force-gradient detected nuclear magnetic resonance. *Appl Phys Lett* 84:5091–5093.
19. Mamin HJ, Budakian R, Chui BW, Rugar D (2005) Magnetic resonance force microscopy of nuclear spins: Detection and manipulation of statistical polarization. *Phys Rev B* 72:024413.
20. Degen CL, *et al.* (2005) Microscale localized spectroscopy with a magnetic resonance force microscope. *Phys Rev Lett* 94:207601.
21. Lin Q, *et al.* (2006) Magnetic double resonance in force microscopy. *Phys Rev Lett* 96:137604.
22. Eberhardt KW, Lin Q, Meier U, Hunkeler A, Meier BH (2007) Sensitive magnetic resonance force imaging of low-gamma nuclei. *Phys Rev B* 75:184430.
23. Degen CL, Poggio M, Mamin HJ, Rugar D (2007) Role of spin noise in the detection of nanoscale ensembles of nuclear spins. *Phys Rev Lett* 99:250601.
24. Kuehn S, Hickman SA, Marohn JA (2008) Advances in mechanical detection of magnetic resonance. *J Chem Phys* 128:052208.
25. Mamin HJ, Poggio M, Degen CL, Rugar D (2007) Nuclear magnetic resonance imaging with 90-nm resolution. *Nat Nanotechnol* 2:301–306.
26. Poggio M, Degen CL, Rettner CT, Mamin HJ, Rugar D (2007) Nuclear magnetic resonance force microscopy with a microwire RF source. *Appl Phys Lett* 90:263111.
27. Caspar DLD (1963) Assembly and stability of the tobacco mosaic virus particle. *Adv Protein Chem* 18:37–121.
28. Klug A (1999) The tobacco mosaic virus particle: Structure and assembly. *Philos Trans R Soc London Ser B* 354:531–535.
29. Taylor KA, Glaeser RM (1974) Electron diffraction of frozen-hydrated protein crystals. *Science* 186:1036–1037.
30. Adrian M, Dubochet J, Lepault J, McDowall AW (1984) Cryo-electron microscopy of viruses. *Nature* 308:32–36.
31. Sleator T, Hahn EL, Hilbert C, Clarke J (1985) Nuclear spin noise. *Phys Rev Lett* 55:1742–1745.
32. Crooker SA, Rickel DG, Balatsky AV, Smith DL (2004) Spectroscopy of spontaneous spin noise as a probe of spin dynamics and magnetic resonance. *Nature* 431:49–52.
33. Müller N, Jerschow A (2006) Nuclear spin noise imaging. *Proc Natl Acad Sci USA* 103:6790–6792.
34. Bertero M, Boccacci P (1998) *Introduction to Inverse Problems in Imaging* (Institute of Physics, Bristol, UK), pp 137–167.
35. Chao S, Dougherty WM, Garbini JL, Sidles JA (2004) Nanometer-scale magnetic resonance imaging. *Rev Sci Instr* 75:1175–1181.
36. Ting M, Raich R, Hero AO (2006) Sparse image reconstruction using sparse priors. *Proceedings of 2006 IEEE Intl. Conf. on Image Processing* (IEEP, Piscataway, NJ).
37. Mamin HJ, Rugar D (2001) Sub-attonewton force detection at millikelvin temperatures. *Appl Phys Lett* 79:3358–3360.
38. Tsang C, *et al.* (2006) Head challenges for perpendicular recording at high areal density. *IEEE Trans Magn* 42:145–149.
39. Haacke EM, Brown RW, Thompson MR, Venkatesan R (1999) *Magnetic Resonance Imaging: Physical Principles and Sequence Design* (Wiley, New York), pp 331–380.